



1 The vulnerability of buildings to a large-scale debris flow and outburst 2 flood hazard chain that occurred on 30 August 2020 in Ganluo, 3 Southwest China

4 Li Wei¹, Kaiheng Hu¹, Shuang Liu¹, Nan Ning^{1,2}, Xiaopeng Zhang^{1,2}, Qiyuan Zhang^{1,2}, Md Abdur Rahim^{1,2,3}

5 ¹ Key Laboratory of Mountain Hazards and Earth Surface Processes, Institute of Mountain Hazards and Environment, Chinese
6 Academy of Sciences, Chengdu 610041, China

7 ² University of Chinese Academy of Sciences, Beijing 100149, China.

8 ³ Department of Disaster Resilience and Engineering, Patuakhali Science and Technology University, Dumki, Patuakhali-8602,
9 Bangladesh

10 Correspondence to: Kaiheng Hu (khhu@imde.ac.cn)

11 **Abstract:** In mountainous areas, damage caused by debris flows is often aggravated by
12 subsequent dam-burst floods within the main river confluence zone. On 30 August 2020, a
13 catastrophic disaster chain occurred at the confluence of the Heixiluo Gully and Niri River in
14 Ganluo County, Southwest China, that consisted of a debris flow, the formation of a barrier lake
15 and subsequent dam breach that flooded the community. This study provides a comprehensive
16 analysis of the damage to buildings resulting from the sequential occurrence of debris flow and
17 dam-burst flood. The peak discharge of the debris flow in the gully mouth reached 1937 m³/s, and
18 the change in the main river channel resulting from the dam-burst flood, which had a peak
19 discharge of 2273 m³/s, resulted in a fourfold increase in the extent of flood inundation compared
20 to an ordinary flood. Three hazard zones were established based on the building damage patterns:
21 (I) primary debris flow burial; (II) secondary dam-burst flood inundation and (III) sequential
22 debris flow burial and dam-burst inundation. Vulnerability curves were developed for Zone (II)
23 and Zone (III) using impact pressures and inundation depths, and a vulnerability assessment chart
24 is presented that contains the three damage categories. This research addresses a gap in the
25 vulnerability assessments of debris flow hazard chains and can support in future disaster
26 mitigation within confluence areas.

27 **Keywords:** Multi-hazard risk, Debris flow, Dam-burst flood, Building damage, Vulnerability
28 analysis.

29 1 Introduction

30 In mountainous areas, debris flows frequently block rivers and form temporary dammed lakes.
31 The subsequent breach of these dammed lakes can result in a vast flash flood (Yan et al., 2020).
32 The hazard chain consisting of debris flows and subsequent dam-burst floods usually devastates
33 residential buildings in confluence zones. For instance, a large-scale debris flow occurred in the
34 Wenjia Gully in Sichuan Province, Southwest China, on 13 August 2010 and completely blocked



35 the Mianyuan River, which formed a dammed lake 1650 m long, 420 m wide, and 12 m deep.
36 Then, the dammed lake breached and caused 7 fatalities and extensive damage to 479 houses (Yu
37 et al., 2013).

38 Multi-hazard analyses that incorporate potential hazard interactions has gained significant
39 attention in recent years (Liu et al., 2015; Gallina et al., 2016; Tilloy et al., 2019; Luo et al., 2023).
40 However, the vulnerability assessments in risk analysis rarely consider the effects of hazard
41 interactions (Luo et al., 2023). Argyroudis et al. (2019) introduced a new methodology for
42 evaluating the vulnerability of transport infrastructure to multiple hazards. This approach is
43 comprised of six steps and includes numerical and fragility models. Progress has been made in
44 assessing the risk of buildings exposed to multiple hazards by considering the interaction between
45 an earthquake and other hazards, such as dam breaks, flash floods, and tsunamis. Korswagen et al.
46 (2019) proposed a methodology for assessing structural damage resulting from coupled hazards
47 and used it to assess the vulnerability of a masonry building subjected to an earthquake and an
48 earthquake-triggered dam break. Furthermore, Park et al. (2012) developed collapse fragility
49 curves for earthquake and tsunami effects using a numerical model. Gautama and Dong (2018)
50 outlined the vulnerability of vernacular stone masonry buildings to the flash floods that occurred
51 after the Gorkha earthquake. Residential buildings in Nepal were found to have up to 300%
52 damage resulting from the combined earthquake and subsequent flash flood. Petrone et al. (2020)
53 simulated the response of reinforced concrete frames to earthquake and tsunami inundation,
54 yielding fragility curves that showed a median decrease of less than 15% in terms of tsunami
55 resistance when exposed to cascading hazards as compared to tsunami-only fragility functions.

56 The evaluation and mitigation of the multiple risks posed by debris flows and dam-burst
57 floods in a confluence zone require a multi-risk analysis that considers hazard interactions and
58 their cumulative effects on building vulnerability. Most studies on debris flow and dam-burst
59 floods mainly focus on numerical simulations and the evolving processes of hazard chains (Nin et
60 al., 2022; Chen et al., 2022), but studies on the vulnerability of building to hazard chains are
61 scarce. The vulnerability of buildings to the cumulative impact of debris flow and flash flood may
62 differ from the sum or sequence of vulnerability resulting from a single debris flow or flash flood
63 (Kappes et al., 2012). The effect that simultaneous hazards have on building vulnerability remains
64 inadequately addressed, with only a few studies available (Kappes et al., 2012). Luo et al. (2020)
65 proposed a framework for developing physics-based vulnerability models for buildings exposed
66 to multiple surges of debris flows. Cumulative damage effects resulting from sequentially
67 occurring debris flows were quantified by assessing the physical damage from primary debris



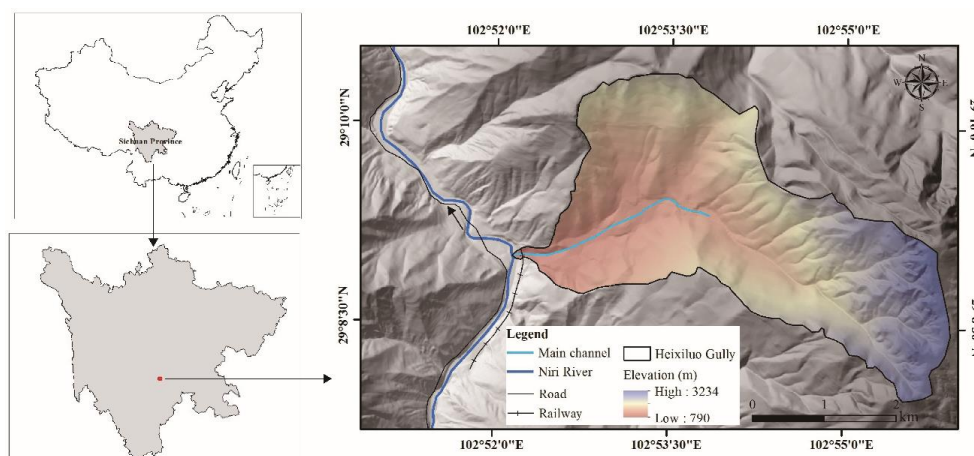
68 flows. However, this approach may not apply directly to the debris flow-dam-burst flood hazard
69 chain.

70 Field investigations have shown that the pattern of damage to buildings in the confluence area
71 of debris flow and flood are not consistent with those from the debris fan or on the floodplain.
72 Debris flow usually causes devastating damage to settlements on the fan, and the subsequent
73 dam-burst flood significantly increases the damage (Xu et al., 2014; Yu et al., 2013). The risk
74 amplification and cumulative effect on building vulnerability resulting from successive debris
75 flows and dam-burst floods are not entirely clear. Therefore, in-depth analysis is essential for
76 assessing the risks posed by the debris flow hazard chain in order to develop a successful
77 emergency management plan.

78 On August 30, 2020, a catastrophic debris flow and dam-burst flood occurred in the Niri
79 River, Ganluo County, Sichuan Province, Southwest China. This study aims to comprehensively
80 analyze the damage to buildings caused by the Heixiluo debris flow-dam-burst flood disaster
81 chain. Firstly, we calculated the dynamic characteristics of the debris flow and outbreak flood
82 damage. We then systematically investigated and summarized the building damage characteristics
83 and analyzed and compared the vulnerability of buildings considering different damage patterns.
84 Finally, we discuss how the damage was amplified by the chain and offer suggestions for hazard
85 mitigation.

86 **2 Study area**

87 The study area is located in Ganluo County, Sichuan Province, Southwest China, which
88 includes the Heixiluo Gully and the confluence area along the Niri River. Ganluo County lies
89 north of the Liangshan Yi Autonomous Prefecture, occupying the alpine canyon zone in the
90 transitional region between the western margin of the Sichuan Basin and the Qinghai-Tibet
91 Plateau (Fig. 1). The geographic boundaries of the study area span from 102°27' to 103°01' east
92 longitude and from 28°38' to 29°18' north latitude. Ganluo County covers a total area of 2150.97
93 km² and had a permanent population of 205,991 at the end of 2020.



94

95

Figure 1 Location of the study area including the Heixiluo Gully and Niri River.

96

Ganluo County consists of an erosional tectonic landform that is defined by two primary structures, namely Sichuan-Yunnan north-south structure and the Qinghai-Tibet Yunnan zeta-type structure. The mountain and river systems flow from south to north due to the folds, uplift, and fractures of the Hengduan Mountains and the strong disruptive effect that widely distributed rivers, undulating hills, ravines, and cliffs have on the study area. The valleys, which are characterized by a V-shaped cross-section, have considerable depths that typically exceed 1000 meters.

103

Folds are ubiquitous in the study area, and the N-S trending Teke fault, Suxiong anticline, and Maanshan anticline are excellent examples of these typical geological structures. These faults were last active during the early and middle Pleistocene and there is no discernible evidence that they were active during the late Quaternary period. The exposed strata in the study area are primarily comprised of Quaternary strata (Q), Presinian Ebian Group (Pteb), and Lower Sinian Suxiong Group (Zas). The upstream area is mainly occupied by sandstone, whereas rhyolite and tuff dominate the main part of the catchment, with slate occupying the left downstream area. The study area is situated in a seismically active region. The peak ground acceleration in the study area is 0.15 g, and the peak period of the seismic response spectrum is 0.45 s. Between 1327 and 1975, nearly 147 $M_s \geq 2.5$ earthquakes were recorded, including 15 $M_s \geq 5.0$ earthquakes with the highest magnitude of 7.5.

114

The Niri River is a first-order tributary of the middle reaches of the Dadu River and flows from south to north and over an elevation range of 1800-2200 for most of the areas. The highest elevation in the river basin is 4700 m, and the lowest elevation is 1170 m. The study area has a subtropical monsoon climate. Summer is humid and hot with abundant rainfall, while winter and

115

116

117



118 spring are warm and dry. The precipitation is distributed unevenly throughout the year. The
119 rainfall is concentrated from April to October, with an average rainfall of 901.9 mm, accounting
120 for 93.14% of the average annual rainfall. The precipitation varies significantly with elevation,
121 with an annual precipitation of 968 mm, and the maximum hourly rainfall and ten-minute rainfall
122 recorded are 40.3 mm and 14.8 mm, respectively.

123 **3 Hazard chain**

124 The Heixiluo Gully is located on the right bank of the Niri River in Suxiong town, Ganluo
125 County (Fig. 1). The coordinates of the gully mouth are 29°09'47"N and 102°52'53"E and the
126 gully extends from the east to the west. The gully covers an area of 13.36 km² and is situated at a
127 moderate elevation on the mountainous landform. The catchment elevation ranges from 3220 m
128 above sea level (a.s.l.) to 760 m a.s.l., with a relative height of 2460 m. The main channel of the
129 gully stretches for 6.93 km, with an average gradient of 355‰. The average slopes for areas
130 above and below 1990 m are approximately 600‰ and 256‰, respectively.

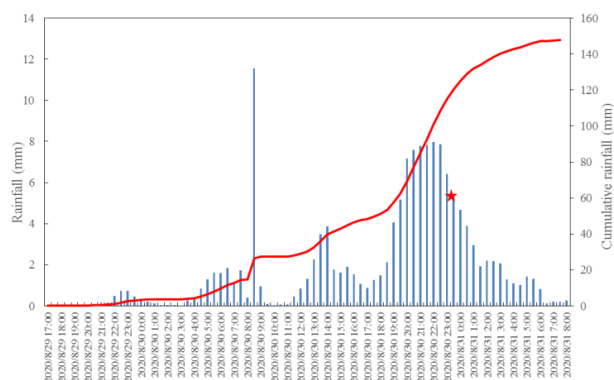
131 The field investigation indicates that the area above elevation of 1990 m where the flash
132 floods provide hydrodynamic conditions are sufficient for forming debris flows. The gradient of
133 the valleys in this area is steep, with an average value of 600 ‰. The transportation zone is
134 mainly located between 820 m and 1990 m in elevation and occupies an area of 5.96 km². The
135 length of the main gully is 4.65 km, and the average gradient of the main gully is 252‰. Two
136 platforms were distributed at altitudes of 1160 m and 1030 m and divided the main channel of the
137 transportation zone into three parts. A narrow channel developed between the platform and the
138 deposition fan at 10230 m. The length and gradient of the channel are approximately 670 m and
139 243‰, respectively.

140 The debris flow was triggered by a once in a century short-term heavy rainfall event.
141 According to the precipitation data from two automated stations located 10 km away, the 24-hour
142 cumulative rainfall from 8:00 on 30 August was approximately 82.8 mm. The rainfall data
143 extracted from the Global Precipitation Measurement (GPM) rainfall product in the Heixiluo
144 Gully showed that the rainfall started on 29 August at 22:00 and lasted until 6:00 on 31 August
145 and delivered a total of 147.2 mm of rain. The hourly rainfall increased to 5.18 mm at 19:30 on
146 30 August, which triggered the debris flow due to the approximately accumulated 61.4 mm of
147 rainfall. The debris flow lasted approximately 40 minutes, and the rainfall intensity reached 6.63
148 mm/h (Fig. 2).



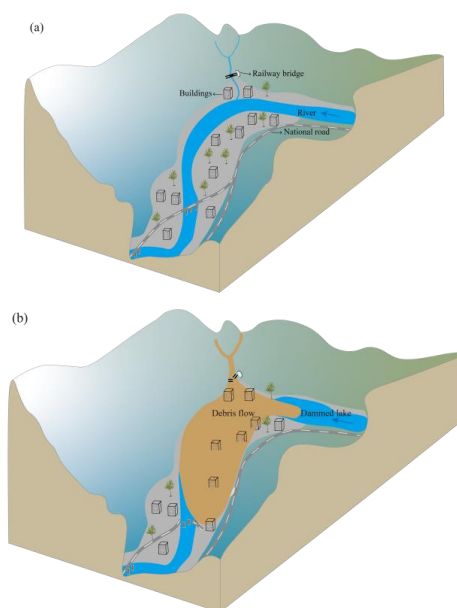
149 Heavy rainfall caused flooding in the Yanrun Hydrometric station (located 15 km upstream
150 from the study area), resulting in a peak discharge of 893 m³/s (He et al., 2020), which was nearly
151 nine times of the average discharge.

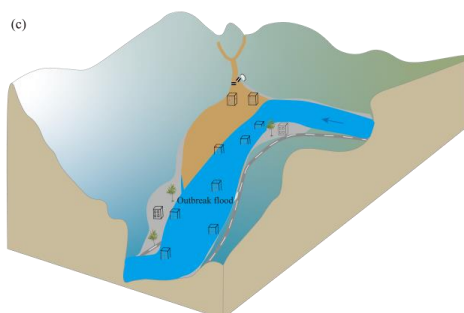
152 The debris flows transported approximately 1,050,000 m³ of material to the Niri River, forming
153 a temporary debris dam that breached after approximately 30 minutes, resulting in a massive flash
154 flood. The debris flow-flash flood event caused significant damages, including the destruction of
155 89 buildings, the Chengdu-Kunming railway bridge near the gully mouth, 1.2 km along national
156 road G245, and 5 highway bridges along the main river (Fig. 3).



157
158
159

Figure 2 Hourly and cumulative rainfall on 29, 30, and 31 August 2020 extracted from the Global Precipitation Measurement (GPM) rainfall product.





160 **Figure 3** Illustration of the multi-hazard chain: (a) river flow before the occurrence of debris flow; (b)
161 debris flow blocks the river and forms a dammed lake that destroys the railway, roads and buildings; (c) the
162 bursting of the dammed lake and buildings and road were damaged or inundated by the flood.

163 **4 Data and methods**

164 We conducted field investigations on the debris flow-flash floods that occurred on 31 August
165 and 3 December 2020. The field survey mainly focused on the main transportation and deposition
166 zones. Interviews, measurements, and aerial photography were conducted to investigate the
167 formation and disaster mechanisms. The geomorphic settings of the Heixiluo Gully and adjacent
168 Niri River were carefully measured and analyzed, including the channel width, deposition and
169 erosion height, channel slope, and particle size distributions. The damage to buildings was also
170 investigated by comparing the drone photos taken before and after the disaster.

171 **4.1 Data collection**

172 The Digital Elevation Modes (DEMs) collected before and after the event were used for
173 hazard chain analysis. The pre-event DEM was converted from a 1:10000 topographic contour
174 map provided by the Sichuan Bureau of Surveying, Mapping, and Geoinformation which had a
175 spatial resolution of 10 m. The post-event DEM of the study area was produced by synthesizing
176 high-resolution aerial images captured by a Dajiang unmanned aerial vehicle (UAV) on 3
177 December 2020. To calibrate the post-event terrain, 10 image control points that were not
178 affected by the disaster were selected, and their elevation values were sampled from the pre-DEM
179 and assigned as input conditions. The mean RMS error of georeferencing of the post-event DEM
180 was within the usable range with a value of 0.1 m.

181 **4.2 Methodology**

182 The dynamic parameters of the debris flow and discharge of the dam-burst flood were
183 calculated by the formulas presented in Table 1.

184



185

Table 1 Models used in parameter calculation for this study

| Category of Calculation | Applied formula | Description parameters |
|--|--|--|
| Debris flow density (Hu et al., 2019) | $\gamma_c = -1320x^7 - 513x^6 + 891x^5 - 55x^4 + 34.6x^3 - 67x^2 + 12.5x + 1.55$ | x is the clay content in the debris flow sample. The average clay content in particles less than 0.005 mm in size accounts for 2.55%. |
| Debris flow peak discharge and velocity (Kang, 1987; Yang, 1985) | $Q = \frac{1}{n_c} AR^{\frac{2}{3}} J^{\frac{1}{2}}$ $n_c = \frac{1}{18.5H^{-0.42}}$ $U = \frac{Q}{A}$ | A is the cross-sectional area, R is the hydraulic radius, J is the channel bed gradient, and n_c is the roughness coefficient for viscous debris flow. The method for calculating n_c was deduced from analysis of viscous debris flows in Huoshao gully in China. |
| Dam-burst flood discharge | $Q = \frac{1}{n} AR^{\frac{2}{3}} J^{\frac{1}{2}}$ | A is the cross-sectional area, Rn is the hydraulic radius, J is the channel bed gradient, and n is the Manning roughness coefficient. The values of A, R, and J were directly measured by the field investigation. |

186 Dam-burst flood hydraulics were simulated by HEC-RAS 5.0.7 (Hydrologic Engineering
 187 Center,2016) using the post-event DEM. The computation procedure employed a one-
 188 dimensional steady flow simulation and assumed a subcritical flow regime. The boundary
 189 conditions are established at all the ends of the river nodes by entering the normal depth value.
 190 The initial conditions were set using the corresponding discharge of the dam-burst flood
 191 estimated at a typical river section using Manning's equation. Manning's n coefficient, expansion,
 192 and contraction coefficients account for flow energy losses in HEC-RAS. The expansion and
 193 contraction coefficients were specified as 0.1 and 0.3, respectively, based on the width of the
 194 channel reaches. Considering the debris flow deposition in the main river, Manning's n values of
 195 the river channel and floodplain were assigned the same value of 0.05. This value is the suggested
 196 value for main channels with clean, winding, pools, shoals, stones, ineffective slopes, and
 197 sections.

198 The dam-breaching peak flow rate was approximately 3.1 times the upstream inflow flood,
 199 with a discharge of 893 m³/s. Therefore, the input discharge for the ordinary flood and dam-burst
 200 flood in the HEC-RAS model were set as 893 m³/s and 2273 m³/s, respectively. Due to the
 201 difficulty of acquiring terrain data for the initial stage of the dam breach, it was assumed that the
 202 peak discharge of the dam-burst flood formed the post-event terrain, which was adopted to
 203 simulate the dam-burst flood. To analyze the impact of debris flows on river dynamics, we also
 204 simulated an ordinary flood unaffected by debris flows using the pre-event DEM. The input
 205 discharge for this simulation was 893 m³/s, which was recorded at upstream hydrological
 206 observation stations located approximately 15 km from Heixiluo Gully. The Manning's n values
 207 for the river channel and floodplain were 0.4 and 0.2, respectively. These values are the suggested
 208 values for main channels that are clean and winding, have some pools and shoals, some weeds



209 and stones, and have flood plains for cultivated areas but are free of crops. The data applied to the
 210 flood calculations are presented in Table 2.

211 **Table 2** Data used in the flood simulation

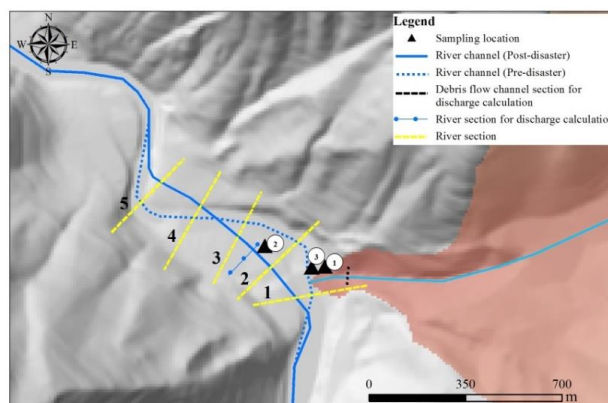
| Floodprocessing | Data | Data source | Manning's n value | Expansion and contraction coefficients |
|-----------------------------------|------------|---|--|--|
| Debris flow dam-burst flood | Topography | Post-event DEM of the river channel | 0.4 (river channel), 0.2 (floodplain) | 0.1 (expansion coefficient) 0.3 (contraction coefficient) |
| | Discharge | Estimated by Manning's equation in a typical section | | |
| Flood not affected by debris flow | Topography | Pre-event DEM of the river channel | 0.5 (river channel and floodplain) | |
| | Discharge | Record in the Yanrun Hydrometric station (located upstream 23 km from Heixiluo Gully) | | |

212 A vulnerability curve was developed to describe the relationship between the hazard intensity
 213 and the degree of damage to the buildings. Following the classification of the damage degrees
 214 proposed by [Hu et al. \(2012\)](#), the degree of damage to buildings caused by multi-hazards was
 215 determined through a comprehensive analysis of photographs taken on site and aerial images
 216 collected over the disaster scene. Hazard intensity parameters were applied, such as flow depth
 217 and impact pressure, with impact pressure calculated as $P = \rho v^2 + 0.5\rho gh$, where P is the
 218 impact pressure, ρ is the flow density, v is the velocity, and h is the flow depth. The deposition
 219 depth of the debris flow was obtained by field investigation, while the velocity was calculated
 220 using the method outlined in **Table 1**. The maximum flow depth and velocity of the flood were
 221 extracted from the HEC-RAS model. A nonlinear regression analysis was conducted using a
 222 logarithmic form expression to relate the vulnerability to the intensity parameters of the hazard.

223 **5 Results**

224 **5.1 Dynamic characteristics of the debris flow and outbreak flood**

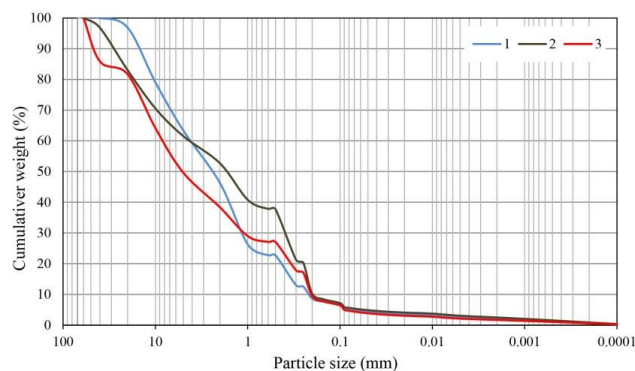
225 Samples of debris particles smaller than 10 cm were taken from three locations (see Fig. 4).
 226 The particle size distribution of the debris flow samples is presented in Fig. 5. The calculated bulk
 227 density of the debris flow is 1.825 g/cm³, which indicates a viscous debris flow ([Kang et al.,](#)
 228 [2004](#)).



229

230

Figure 4 Distribution of river and debris flow channel sections and debris flow sampling locations.



231

232

Figure 5 Particle size distribution of debris flow samples.

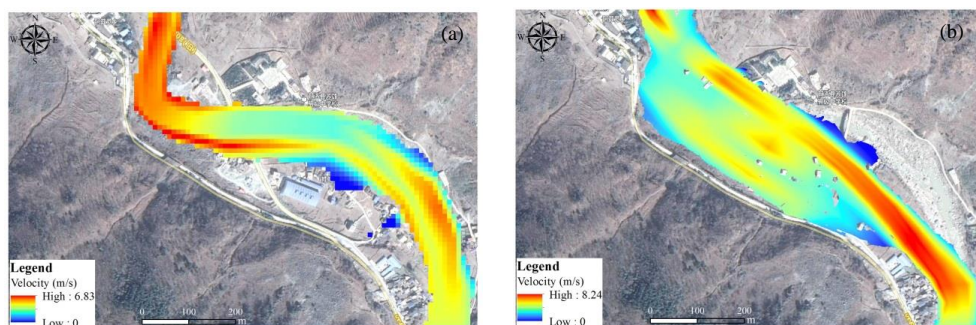
233 The debris flow destroyed the Chengdu-Kunming railway bridge situated at the gully mouth
234 and had a flow depth of approximately 5 m and a section area of approximately 150 m². The
235 estimated peak discharge at the gully mouth using Kang's equation (1987) was 1611 m³/s, which
236 resulted in a high impact pressure of 255 kPa.

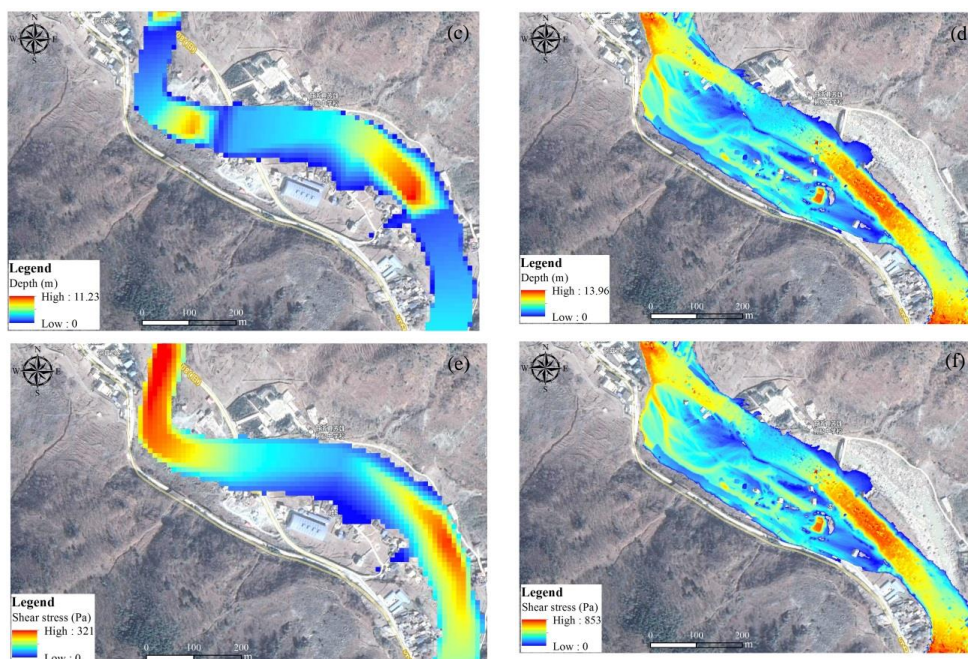
237 The debris flow lasted for approximately 40 minutes and transported approximately
238 1,050,000 m³ of sediment downstream. The deposition zone extended from the gully mouth to the
239 floodplain of the Niri River, covering a length of 320 m (Fig. 3). The area measured from the
240 UAV image was approximately 0.15 km². The thickness of the sediment deposits ranged from 5
241 m to 15 m, with an average value of 7 m. The debris flow flushed into the main river and blocked
242 the Niri River. The river channel was filled with sediment, which lead to the formation of a
243 dammed lake that raised the water level by 7-8 m. After 30 minutes, the unstable dammed lake
244 breached, which resulted in a massive flash flood.



245 The outburst of the debris flow lake caused a sharp increase in flood peak discharge. To
246 analyze the dynamic characteristics of the flood caused by the dam burst, we first used Manning's
247 hydraulic formula for open channel flow (presented in Table 1) to calculate the peak discharge.
248 Then, we selected empirical formulas for dam-burst floods to verify the discharge. A typical
249 section adjacent to buildings damaged by the flood was chosen for the calculation (Fig. 4). Based
250 on flood traces on the outer walls of buildings and the damaged height of buildings, the flood
251 depth was estimated to be 6 m. The cross-sectional area and hydraulic radius were calculated
252 according to the section geometry and channel profile. The channel bed gradient was determined
253 based on the longitudinal channel profile. The resulting peak discharge was 2737 m³/s. Field
254 investigation revealed that the height of the debris flow dam was approximately 12 m. The
255 volume of the barrier lake was calculated based on the terrain data collected before the disaster.
256 The peak discharge was estimated using the empirical formula proposed by Costa (1985)
257 ($Q_{max} = 1.122V_s^{0.57}$, where V_s is the barrier lake volume), which produced a result of 2273
258 m³/s that is close to the result obtained by Manning's equation.

259 The temporal distributions of flood depth, velocity, and shear stress in the two scenarios are
260 presented in Fig. 6. The flood completely submerged all buildings on the left bank near the
261 middle of the river channel, and the buildings on the river terrace on the right bank were strongly
262 eroded. The maximum water depth and velocity of the dam-burst flood were 13.96 m and 8.24
263 m/s, respectively, which were 1.24 and 1.31 times higher than those of the ordinary flood,
264 respectively. The maximum shear stress of the flood in the main channel increased sharply from
265 320 Pa to 853 Pa, indicating a 2.67-fold increase compared to the ordinary flood. For the ordinary
266 flood scenario, the water depth and velocity were high in the channel and decreased in the
267 floodplain. In contrast, the high velocity and shear stress zones that resulted from the dam-burst
268 flood were mainly distributed in the main channel and along the left bank, indicating that the
269 material deposited by the debris flow and the original river bank are highly susceptible to erosion.



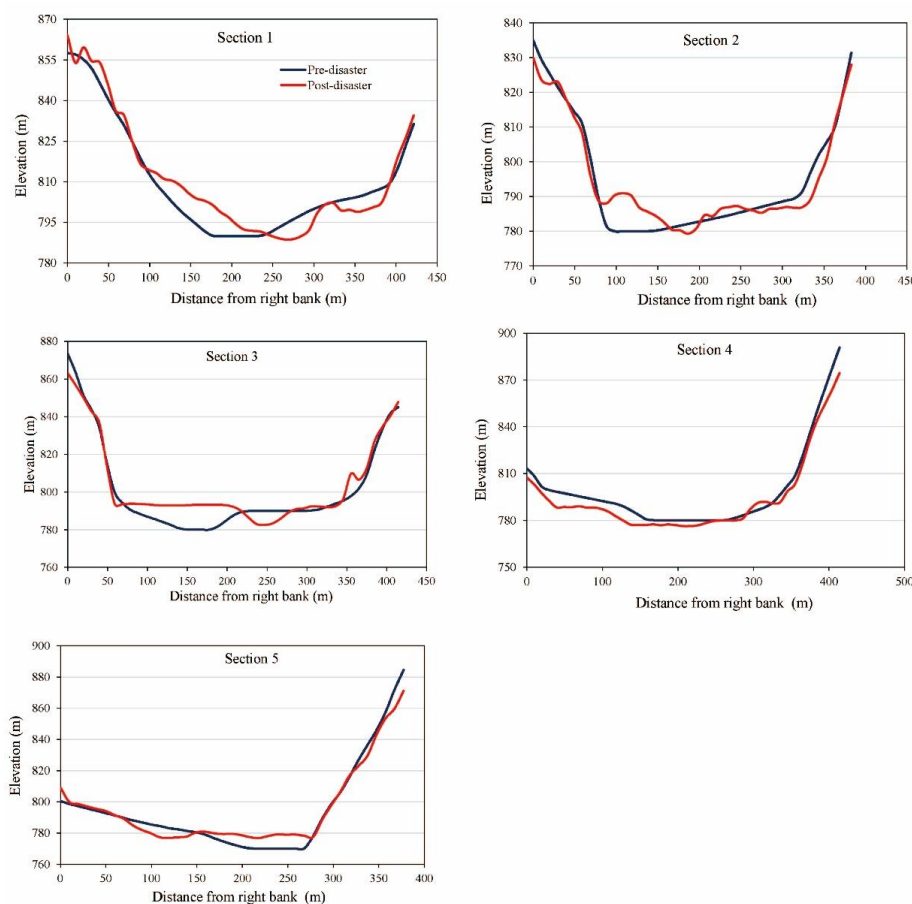


270 **Figure 6** Distribution of depth, velocity, and shear stress of ordinary flood and dam-burst flood: (a)
271 Maximum velocity distribution of ordinary flood; (b) Maximum velocity distribution of dam-burst
272 flood;(c) Maximum depth distribution of ordinary flood;(d) Maximum depth distribution of dam-burst
273 flood;(e) Maximum shear stress distribution of ordinary flood;(f) Maximum shear stress distribution of
274 dam-burst flood.

275 The critical shear stress for bedload transport in the gravel-bed river is determined by the
276 equation $\theta = \frac{\tau}{(\rho_s - \rho)gD} = 0.04$, where θ is the critical shear stress, τ is the bed shear stress, ρ_s is the
277 soil mass density, ρ is the water mass density, g is the gravitational acceleration, and D is the
278 sediment diameter (Petit et al., 2015). The dam-burst flood had the potential to transport large
279 boulders up to 1.3 m in diameter, while an ordinary flood could only move gravel up to 0.49 m in
280 diameter. Such high shear stress also demonstrated the strong erosional ability of the dam-burst
281 flood, which seriously scoured the debris sediment deposit and original riverbank, transporting
282 coarse gravel and forming a new straight river channel. The new channel is straighter and steeper
283 than the original channel, raising the bed of the Niri River by 1-17 m and burying buildings up to
284 1 km downstream of Heixluo Gully. The channel length shortened from 1010 m to 842 m, and the
285 channel gradient increased from 1.71% to 2.72%. The change in the river channel led to an
286 inundation area that deflected to the left. Buildings built on the original left riverbank were first
287 impacted by debris flow and subsequently destroyed by the flood. The river terrace on the
288 original right bank was strongly eroded by the flood, leading to the collapse and demolition of
289 buildings. Five river sections (Section 1 to Section 5) were selected to analyze the terrain changes



290 (see Fig. 4). From Section 1 to Section 3, the main channel varied from the right bank to the left
291 bank with a distance between 40 m and 100 m, the average width of the new river channel was 50
292 m, and the vertical distance between the new riverbed and floodplain was 11.23 m. In Section 5,
293 the channel migrated from the left bank to the right bank due to the severe erosion of the original
294 river terrace and had a maximum depth of 10 m (Fig. 7). The channel width increased to
295 approximately 100 m, and the channel depth decreased to less than 5 m.



296

297

Figure 7 Cross-section profile before and after the disaster.

298 **5.3 Damage patterns of buildings**

299 The debris flow-outburst flood hazard chain caused damage to 89 buildings, a 1.2 km stretch of
300 national road G245, and 5 highway bridges along the main river. The evolution of this hazard
301 chain occurred in two phases. First, the debris flow blocked the main river and formed a barrier
302 dam and dammed lake, which was, second, followed by the outburst of the lake that led to the



303 subsequent flooding and inundation. During the first phase, a significant amount of sediment was
304 transported by the debris flow to the confluence area and deposited in the river channel, which
305 formed a barrier lake with a volume of 857,504 m³. The barrier lake breached completely only
306 approximately 30 minutes later, leading to a highly energetic flood that caused serious erosion of
307 the riverbank and the formation of the outburst flood, a new straight river channel.

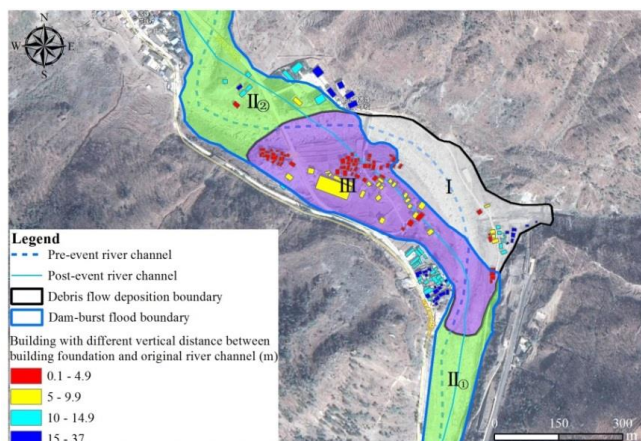
308 Fig. 8 illustrates the boundary of debris flow deposition and dam-burst flood inundation. The
309 debris flow deposition boundary was determined via a field investigation and compared with
310 results obtained from a liquid–solid two-phase model, which takes into account the effects of
311 runoff and entrainment (Li et al., 2022). The flooding boundary was obtained by combining the
312 results of the HEC-RAS simulation with field survey data. The confluence area was heavily
313 impacted by the debris flow, resulting in the transportation of a significant amount of solid
314 materials over an area of 0.157 km². As a result, the majority of the village’s buildings were
315 inundated by the debris flow. The dam-burst flood caused serious damage to buildings by
316 flushing a large volume of debris flow sediment and riverbank material downstream.

317 Three hazard zones are identified based on the boundary of the debris flow and dam-burst
318 flood, as shown in Fig. 8 and Fig. 9. The damage patterns of buildings in the different hazard
319 zones can be classified into three categories, namely, (I) buildings only buried by debris flow; (II)
320 buildings only inundated by dam-burst flood; and (III) buildings sequentially buried by debris
321 flow and inundated by dam-burst flood. Zone (I) is situated near the Heixiluo gully mouth, where
322 the debris flow transported a large volume of sediment and seriously eroded the sidewall and bed
323 of the channel, expanding the channel’s width from 10 m to 40 m. All buildings were inundated
324 by sediment to a depth of over 6 m.

325 Zone (II) is subdivided into two subzones, Zone (II) ① and Zone (II) ②, based on the spatial
326 location. Zone (II) ① is situated in the upstream reach of the Niri River, near the debris flow dam,
327 and is mainly inundated by the static water of the dammed lake (Fig. 9(b)). Zone (II) ② lies on the
328 right bank of the downstream reach of the Niri River, outside the debris flow fan. The original
329 right riverbank in Zone (II) ② was a terrace 10 m high that was severely scoured by the highly
330 energetic flood with a shear stress greater than 450 Pa. The entire terrace was cut off, and a new
331 channel was formed across the middle area (Fig. 9(c)). The erosion area on the river terrace
332 measures approximately 1800 m² with a length of 300 m and a width of 60 m. Two buildings
333 situated on the upper part of the river terrace collapsed and disintegrated due to the impact of the
334 flood (part (a) in Fig. 9(d)). A three-story building was partially destroyed due to foundation
335 erosion. The buildings on the lower part of Zone (II) ② were simultaneously buried by the
336 sediment transported by floods and inundated by floodwater (part (b) in Fig. 9(d)).



337 Zone (III) is primarily located on the left bank of the original river and the lower part of the
338 debris flow fan. The original river channel is filled with debris up to a depth of 10 m. The debris
339 flow transported sediment across the raised riverbed into villages and formed a slope that was
340 high on the right and low on the left in the confluence area. Then, the flood breached the debris
341 flow dam and severely eroded the deposited debris and the original floodplain surface, resulting
342 in a new straight channel. The buildings on the left bank of the river, which were buried by the
343 debris flow, were sequentially impacted by the dam-breach flood. The flood heavily damaged
344 buildings near the new river channel, and floodwater from the channel was observed to always
345 inundate the buildings. Notably, the boundaries of the different damage zones are not static. The
346 extent of the damage zone is not the same for other confluence areas; it is determined by the
347 dynamic characteristics of hazards and is also influenced by the local terrain.



348
349 **Figure 8** Inundation boundary of debris flow and dam-burst flood and spatial division of the hazard zone
350 based on building damage patterns: (I) buried by debris flow; (II) inundated by dam-burst flood; (III)
351 buried by debris flow and the inundated by dam-burst flood.

352 A total of 110 buildings in the village were impacted by the multi-hazards, accounting for
353 69.62% of the total buildings. Among them, 75 buildings located in Zone (III) were impacted by
354 the debris flow and flood in succession, which accounted for 47.47% of the total buildings. In
355 contrast, buildings destroyed by the debris flow in Zone (I) and dam-burst flood in Zone (II)
356 accounted for only 16.46% and 5.70% of the total buildings, respectively (Table 3). Overall, the
357 number of buildings within the debris flow deposition boundary and flood inundation boundary is
358 101 and 84, respectively, accounting for 63.92% and 53.16% of the total buildings in the village.
359



360
 361
 362
 363

Figure 9 Spatial distribution of the three hazard zones before and after the disaster: (a) before the disaster; (b) (c) (d) after the disaster.

Table 3 Statistics of buildings damaged by the debris flow and dam-burst flood

| Damage pattern | (I) Buried by debris flow | (II) Inundated by dam-burst flood | (III) Buried by debris flow and inundated by dam-burst flood sequentially | Sum |
|---|---------------------------|-----------------------------------|---|-------|
| Total number of buildings destroyed | 26 | 9 | 75 | 110 |
| The proportion of damaged buildings to the total buildings in the village (%) | 16.46 | 5.70 | 47.47 | 69.62 |

364

365 The impact force of fluvial sediment transport is greatly influenced by the relative distance of
 366 buildings to channels (Wei et al., 2022). Buildings that are close to the channel are always more
 367 vulnerable to damage than those located farther away from the river. During the hazard chain, a
 368 total of 84 buildings in Zone (II) and Zone (III) were impacted by the dam-burst flood (Fig. 10).
 369 To assess the influence of building distance from the river channel, we analyzed the vertical
 370 distances between the damaged building foundation and the original river channel based on pre-
 371 event terrain (Table 4). We found that 67.86% of all damaged buildings were within 5 m of the
 372 channel, while 23.81% of all damaged buildings were between 5 m and 10 m of the original
 373 channel. Buildings that were located at distances greater than 10 m only accounted for 8.33% of



374 the total damaged buildings. In contrast, the average vertical distance of undamaged buildings
375 was 15.3 m, with a minimum value of 11.4 m.

376 **Table 4** Statistics of the vertical distance between the damaged building foundation and
377 original river channel within the whole flooding boundary

| The vertical distance between the building foundation and original river channel (m) | (0, 5) | (5,10) | (10,16) | Sum |
|--|--------|--------|---------|-----|
| Total number of buildings destroyed | 57 | 20 | 7 | 84 |
| The proportion of damaged buildings to the total (%) | 67.86 | 23.81 | 8.33 | 100 |

378 **5.4 Vulnerability analysis of the buildings**

379 Most of the buildings in the village were completely buried by sediments or collapsed with no
380 visible remains. To construct vulnerability curves, 29 damaged buildings with brick-concrete
381 structures located in the three hazard zones were selected (Fig. 9(c), Fig. 10). Of these, 2
382 buildings were located in Zone (I), 7 buildings were located in Zone (II), and the rest were
383 distributed throughout Zone (III).

384 The building characteristics and hazard intensity are presented in Table 5. The two buildings
385 in Zone (I) were buried by debris flow with a thickness greater than 5 m. In Zone (III), buildings
386 located near the debris flow dam (such as buildings 3, 4, and 5) were first buried by the debris
387 flow and then inundated by water from the dammed lake for 30 minutes. These buildings were
388 then impacted by the dam-burst flood. Additionally, buildings near the new river channel suffered
389 greater impact pressure than other buildings. For example, the residual broken structures of
390 buildings 7 and 8 were heavily damaged by the direct impact of the flood in the vertical direction.
391 The walls of the two buildings were severely abraded by impact pressures of 75.7 kPa and 71.1
392 kPa, respectively. Additionally, the foundations of the two buildings were partially scoured by
393 floods with high shear stresses of 562 Pa and 553 Pa, respectively.

394 Buildings located in Zone (II) were only severely impacted by the dam-burst flood. For instance,
395 the foundation of the three-story school building (building 27) was severely eroded by the flood
396 to a scour depth of 1 m, and the floors on the right were collapsed. There was no evidence on the
397 walls of the building that the debris flow had abraded the structure. The velocity and shear stress
398 of the flood in this location were 5.3 m/s and 463 Pa, respectively. Buildings 23-27, which were
399 close to the new river channel, were thoroughly buried by the sediment transported by the flood
400 and inundated by floodwater.

401



Figure 10 Buildings with the different degree of damages within three hazard zones.

402
 403
 404
 405
 406
 407
 408
 409
 410
 411
 412
 413
 414
 415
 416
 417

The vulnerability curve in Zone (II) and Zone (III) was developed by summing up the damage caused by the multiple hazards and impact pressure (Fig. 11). Logistic functions were proposed separately for the two hazard zones, and the corresponding determination coefficient (R^2) and root mean square error (RMSE) were also obtained. The determination coefficients of the two regression curves in Zone (III) have a higher R^2 . The RMSEs of the curves in Zone (II) and Zone (III) are 0.08 and 0.14, respectively. The correlation between vulnerability and inundation depth in the two zones is shown in Fig. 12, with an R^2 lower than impact pressure ($R^2=0.30$ for Zone (II) and $R^2=0.41$ for Zone (III)). Building vulnerability increases with increasing hazard intensity, and the trend is similar in the two zones. For the same impact pressure and inundation depth, the damage to buildings in Zone (II) is greater than that in Zone (III). The threshold of the impact pressure in Zone (II) and Zone (III) where vulnerability is equal to 1 is 88 kPa and 106 kPa, respectively, which is much greater than that of the three functions.

Table 5 Database of the damaged buildings

| Building | Debris flow deposition depth (m) | Debris flow velocity (m/s) | Debris flow impact pressure (kPa) | Flood depth (m) | Flood velocity (m/s) | Flood impact pressure (kPa) | Damage ratio | Hazard zone |
|----------|----------------------------------|----------------------------|-----------------------------------|-----------------|----------------------|-----------------------------|--------------|-------------|
| 1 | 5 | 3.9 | 39.7 | | | | 0.9 | I |



| | | | | | | | | |
|----|-----|-----|------|-----|-----|------|-----|-----|
| 2 | 6 | 4.1 | 46.0 | | | | 1 | I |
| 3 | 1 | 2.6 | 11.8 | 1.2 | 1.0 | 7.0 | 0.7 | III |
| 4 | 2 | 3.1 | 19.4 | 1.3 | 2.0 | 10.3 | 0.6 | III |
| 5 | 2 | 3.1 | 19.4 | 1.3 | 2.3 | 11.6 | 0.6 | III |
| 6 | 7 | 4.2 | 52.2 | 3.7 | 4.3 | 36.8 | 0.8 | III |
| 7 | 1.5 | 4.1 | 23.9 | 6.7 | 6.5 | 75.5 | 1 | III |
| 8 | 6 | 3.4 | 41.2 | 6.3 | 6.3 | 71.1 | 1 | III |
| 9 | 5 | 3.9 | 39.7 | 1.0 | 2.0 | 8.8 | 0.7 | III |
| 10 | 3 | 3.4 | 26.5 | 2.1 | 4.1 | 27.3 | 0.6 | III |
| 11 | 2 | 3.1 | 19.4 | 6.4 | 6.7 | 76.6 | 1 | III |
| 12 | 2 | 3.1 | 19.4 | 6.3 | 6.0 | 67.1 | 1 | III |
| 13 | 2 | 3.1 | 19.4 | 0.9 | 3.6 | 17.6 | 0.7 | III |
| 14 | 4 | 3.7 | 33.2 | 4.4 | 5.9 | 56.3 | 1 | III |
| 15 | 5 | 3.9 | 39.7 | 3.6 | 5.1 | 43.3 | 0.7 | III |
| 16 | 0.5 | 2.2 | 7.3 | 0.7 | 1.5 | 5.8 | 0.4 | III |
| 17 | 1 | 2.6 | 11.8 | 1.2 | 0.8 | 6.5 | 0.3 | III |
| 18 | 0.5 | 2.2 | 7.3 | 3.0 | 4.6 | 35.7 | 1 | III |
| 19 | 0.5 | 2.2 | 7.3 | 3.9 | 5.0 | 44.4 | 1 | III |
| 20 | 1 | 2.6 | 11.8 | 2.4 | 3.8 | 26.0 | 0.7 | III |
| 21 | 1 | 2.6 | 11.8 | 2.4 | 4.1 | 28.1 | 0.9 | III |
| 22 | 0.5 | 2.2 | 7.3 | 3.5 | 4.7 | 39.5 | 1 | III |
| 23 | | | | 5.3 | 5.4 | 55.3 | 0.8 | II |
| 24 | | | | 1.6 | 3.2 | 18.2 | 0.7 | II |
| 25 | | | | 4.7 | 4.9 | 47.2 | 0.8 | II |
| 26 | | | | 3.7 | 3.6 | 31.5 | 0.7 | II |
| 27 | | | | 3.7 | 5.3 | 45.8 | 0.9 | II |
| 28 | | | | 4.5 | 4.4 | 41.0 | 1 | II |
| 29 | | | | 5.1 | 5.1 | 51.4 | 1 | II |

418

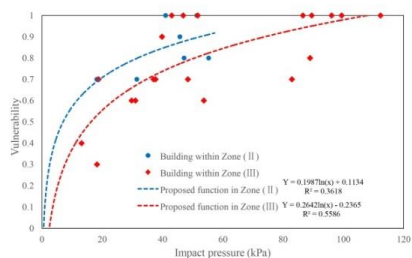


Figure11 Proposed vulnerability functions based on the impact pressure in Zone (II) and Zone (III).

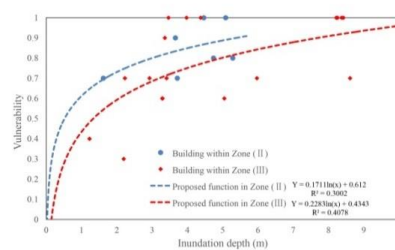


Figure12 Proposed vulnerability functions based on the inundation depth in Zone (II) and Zone (III).



419 The vulnerability curves proposed for Zone (II) and Zone (III) were compared to the three
420 functions used in debris flow risk assessment (Fig.13, Fig.14). The functions developed by [Quan](#)
421 [et al. \(2011\)](#) and [Kang et al. \(2016\)](#) were calculated based on damage done to brick masonry and
422 nonreinforced concrete structures that had been impacted by the debris flows in South Korea and
423 Italy, respectively. The vulnerability curve proposed by [Zhang et al. \(2018\)](#) was developed for
424 buildings with brick-concrete structures from the Zhouqu debris flow event in China. The slope
425 of the two proposed vulnerability curves based on impact pressure is smaller than those of the
426 three curves. When the impact pressure is less than 20 kPa, the proposed curves show a similar
427 increasing trend compared to the three functions. However, when the impact pressure is greater
428 than 20 kPa, the slope of the two proposed vulnerability curves is much smaller than those of the
429 three curves. For the curves based on inundation depth, when the depth is less than 2 m, the slope
430 is steeper than that of [Quan et al. \(2011\)](#) and [Zhang et al. \(2018\)](#) and slower than that of [Kang et](#)
431 [al. \(2016\)](#). When the depth is greater than 2 m, the damage increases slower than the curves of
432 [Quan et al. \(2011\)](#) and [Zhang et al. \(2018\)](#). This disparity may be attributed to the different
433 damage patterns and structures of the buildings in this study. The three vulnerability functions
434 were generated for a single debris flow event, whereas the mechanisms by which buildings
435 impacted by floods fail is not the same when those buildings are subjected to a debris flow. The
436 structures of most buildings in the study area are tougher than those in the three events, and
437 nearly half of the buildings had been recently built by a more professional construction team. For
438 example, the newly built four buildings 6, 9, 10, and 15 were not completely damaged by hazard
439 chain under impact pressures greater than 40 kPa.

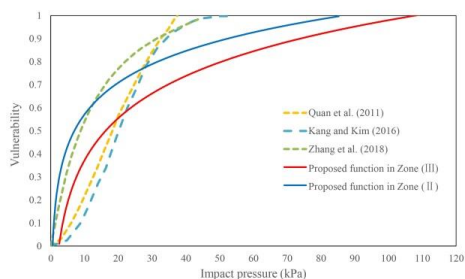


Figure 13 Comparison of the building vulnerability functions with the impact pressure functions proposed by [Quan et al. \(2011\)](#), [Kang et al. \(2016\)](#), and [Zhang et al. \(2018\)](#).

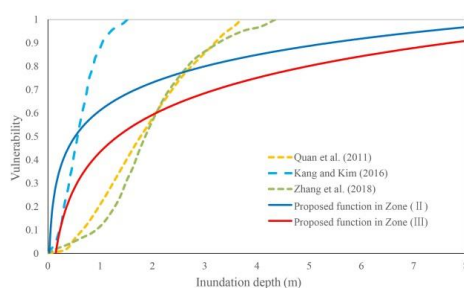
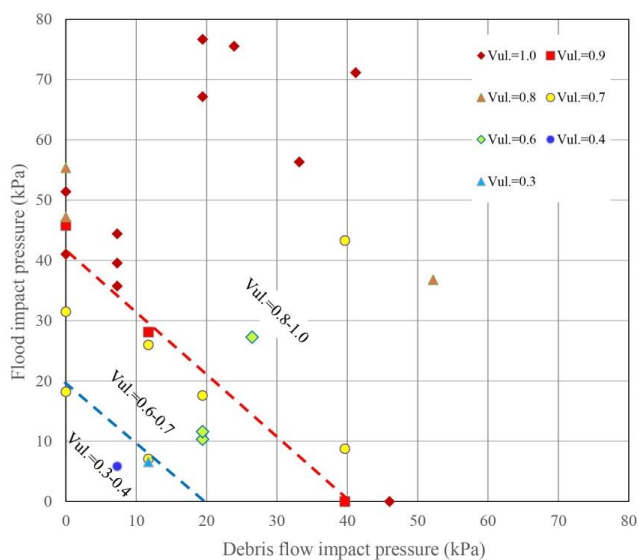


Figure 14 Comparison of the building vulnerability functions with the inundation depth proposed by [Quan et al. \(2011\)](#), [Kang et al. \(2016\)](#), and [Zhang et al. \(2018\)](#).

440 The building damage distribution chart shows building damage plotted as a function of debris
441 flow and flood impact pressure (see Fig. 15). The figure includes aggregated damage to buildings



442 impacted by the sequentially occurring hazards in Zone (III) and damage caused by a single
443 hazard in Zone (I) and Zone (II). Damage is divided into three categories based on the threshold
444 impact pressure: slight damage (0.3-0.4), moderate damage (0.6-0.7), and heavy and complete
445 damage (0.8-1.0). Heavy damage occurs at impact pressures greater than 40 kPa, while slight
446 damage occurs below 20 kPa. Moderate damage occurs at impact pressures between 20 kPa and
447 40 kPa. The threshold impact pressure is compared with that proposed by [Hu et al. \(2012\)](#) and
448 [Zanchetta et al. \(2004\)](#), which were derived from a single debris flow disaster in China and Italy,
449 respectively. Although the detailed definition of the damage scales differs, the threshold of the
450 impact pressure for buildings at the slight, heavy, and complete damage scales is generally larger
451 than that for the brick-concrete structures presented in [Hu et al. \(2012\)](#) and smaller than that for
452 the reinforced concrete frames also presented in [Hu et al. \(2012\)](#) and the masonry structures with
453 basements presented in [Zanchetta et al. \(2004\)](#). A similar trend for the threshold of the impact
454 pressure for buildings with a moderate damage scale can be observed.



455
456 **Figure 15** Accumulation of building damage due to debris flow and dam-burst flood. The damage
457 distribution is based on the debris flow and flood impact pressure (Vul. refers to vulnerability).

458 The building damage distribution chart remains a valid tool for assessing the vulnerability of
459 buildings affected by debris flows and flash floods, despite not incorporating all damage ratios.
460 However, some limitations and uncertainties exist within the vulnerability functions. For instance,
461 calculating a single average impact pressure value prebuilding for building clusters introduces
462 uncertainty, as water depth and velocity differ significantly at different sides of the building due



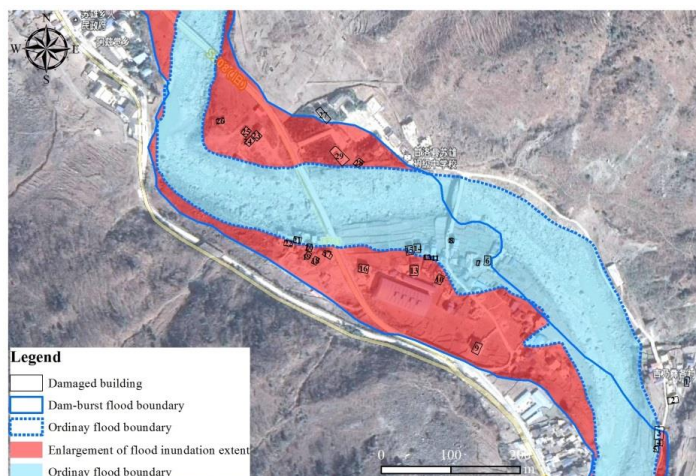
463 to the shielding effect (Hu et al., 2012; Arrighi et al., 2020). Furthermore, the building's geometry,
464 direction, orientation, and maintenance condition are not considered in the vulnerability analysis.
465 The amplification of debris flow damage is due to subsequent flooding in time and space.
466 Aggregated damage (i.e., damage caused by both debris flows and floods) is applied in the
467 vulnerability analysis for areas that are successively struck by debris flows and floods. However,
468 the amplified damage effect of the dam-burst flood on debris flow was not accurately quantified
469 because of the absence of a database containing information regarding the damage done by the
470 debris flow before the dam burst. As a result, more detailed data are needed to assess the
471 cumulative impact of hazard chains on building vulnerability.

472 **6 Discussion**

473 **6.1 Expansion of flood inundation extent**

474 As a result of the confluence zone's location on a river bend, the dam-burst flood typically
475 flows in a straight direction and creates a new straight channel when the river channel becomes
476 completely blocked. This channel translocation leads to a larger flooded area and causes more
477 severe damage to buildings on the floodplain. The flood inundation zones in the village expanded
478 to 110^5 m², which is up to 4 times the area of an ordinary flood due to flood amplification (Fig.
479 16). In the expanded inundation zone, 41 buildings, a traffic road spanning 410 m, and farmland
480 with an area of 10×10^4 m² were submerged. The buildings located in the middle of the inundation
481 zones suffered the most severe damage due to the floodwater's high scouring capability and
482 sediment transport capacity. Many buildings near the flow collapsed, and most structures were
483 carried away by the water current.

484 Table 6 presents a comparison of the dynamic characteristics and damage increments between
485 ordinary and dam-burst floods in different locations. The damage increment is calculated based
486 on the proposed function in Zone II and is the ratio of the damage caused by the two floods.
487 Buildings 6, 7, 8, 14, and 15 were situated close to the new river channel, and the bed shear stress
488 and impact pressure increased up to 24.67 times and 6.76 times that of an ordinary flood,
489 respectively. Building 21 was constructed near the original channel, and the increase of bed shear
490 stress and impact pressure was smaller than in the other buildings. Overall, the average bed shear
491 stress and impact pressure increased by 16.83 and 4.24 times, respectively, due to flood
492 amplification. The average damage to the six buildings located near the new channel increased by
493 119% due to the lake created by the debris flow barrier.



494
 495

Figure 16 The inundation extent of ordinary floods and dam-burst floods.

496 **Table 6** Comparison of dynamic characteristics and degree of damage between ordinary floods and dam-
 497 burst floods in different locations

| Location | The ratio of dam-burst flood to ordinary flood | | | | |
|---------------|--|----------|------------------|-----------------|---------------|
| | Depth | Velocity | Bed shear stress | Impact pressure | Damage degree |
| Building 6 | 2.00 | 1.78 | 9.88 | 2.46 | 1.19 |
| Building 7 | 3.49 | 3.20 | 24.67 | 5.54 | 1.36 |
| Building 8 | 3.12 | 2.14 | 17.45 | 3.79 | 1.26 |
| Building 14 | 6.49 | 2.64 | 24.43 | 6.76 | 1.45 |
| Building 15 | 6.30 | 2.20 | 18.58 | 5.34 | 1.40 |
| Building 21 | 2.95 | 1.08 | 5.96 | 1.55 | 1.09 |
| Average value | 4.05 | 2.17 | 16.83 | 4.24 | 1.19 |

498 **6.2 Damage aggravation due to hazard chain**

499 The debris flow-outburst flood hazard chain extends the damage in time and space. The
 500 blockage of the river results in upstream inundation and downstream outburst flood, exacerbating
 501 the damage caused by the debris flow. To assess the amplified damage effect on building
 502 vulnerability, impact pressure functions proposed by [Quan et al. \(2011\)](#) and [Zhang et al. \(2018\)](#)
 503 were applied to calculate the damage caused by the debris flow. Table 7 presents a comparison of
 504 the calculated damage with the aggregated damage caused by the debris flow and outbreak flood.
 505 Except for buildings 6, 9, 10, and 15, the damage to buildings increased markedly due to the
 506 cumulative effect that the dam-burst flood had on building vulnerability. On average, the damage
 507 increased by 4.8 times and 5.4 times compared to the damage results calculated by [Quan et al.](#)



508 (2012) and Zhang et al. (2018), respectively. The aggravated damage is up to 20 times that caused
 509 by debris flow alone.

510 **Table 7** Comparison of damage caused by debris flow with the cumulative damage

| Building | Debris flow inundation depth (m) | Aggregated damage ratio (D1) | Damage ratio calculated by Quan et al. (2012) (D2) | Damage ratio calculated by Zhang et al. (2018) (D3) | Ratio of D1 to D2 | Ratio of D1 to D3 |
|----------|----------------------------------|------------------------------|--|---|-------------------|-------------------|
| 3 | 1 | 0.7 | 0.2 | 0.12 | 3.5 | 5.8 |
| 4 | 2 | 0.6 | 0.57 | 0.56 | 1.1 | 1.1 |
| 5 | 2 | 0.6 | 0.57 | 0.56 | 1.1 | 1.1 |
| 6 | 7 | 0.8 | 1 | 1 | 0.8 | 0.8 |
| 7 | 1.5 | 1 | 0.4 | 0.3 | 2.5 | 3.3 |
| 8 | 6 | 1 | 1 | 1 | 1 | 1 |
| 9 | 5 | 0.7 | 1 | 1 | 0.7 | 0.7 |
| 10 | 3 | 0.6 | 1 | 0.86 | 0.6 | 0.7 |
| 11 | 2 | 1 | 0.57 | 0.56 | 1.8 | 1.8 |
| 12 | 2 | 1 | 0.57 | 0.56 | 1.8 | 1.8 |
| 13 | 2 | 0.7 | 0.57 | 0.56 | 1.2 | 1.3 |
| 14 | 4 | 1 | 1 | 0.96 | 1 | 1.0 |
| 15 | 5 | 0.7 | 1 | 1 | 0.7 | 0.7 |
| 16 | 0.5 | 0.4 | 0.05 | 0.05 | 8 | 8 |
| 17 | 1 | 0.3 | 0.2 | 0.12 | 1.5 | 2.5 |
| 18 | 0.5 | 1 | 0.05 | 0.05 | 20 | 20 |
| 19 | 0.5 | 1 | 0.05 | 0.05 | 20 | 20 |
| 20 | 1 | 0.7 | 0.2 | 0.12 | 3.5 | 5.8 |
| 21 | 1 | 0.9 | 0.2 | 0.12 | 4.5 | 7.5 |
| 22 | 0.5 | 1 | 0.05 | 0.05 | 20 | 20 |

511 6.3 The implication of hazard mitigation

512 In recent years, the hazard chain of debris flows and outburst floods has become more frequent
 513 in high mountain regions due to the impact of climate change and earthquakes (Chen et al., 2022).
 514 The damage caused by the primary debris flow can be intensified and enlarged due to the
 515 successive dam-burst flood.

516 Risk assessment for debris flow-outburst flood hazard chains is crucial to mitigate the damage
 517 posed to structures in the confluence zone. Risk analysis should incorporate both the debris flow
 518 initiation mechanism and the mechanism that generates the dam-burst flood (Chen et al., 2022). A
 519 detailed investigation should be conducted for the exposed elements in the confluence zone and in



520 both the upstream and downstream reaches of the river. Based on the disaster transformation
521 process and the failure mechanisms of structures, hazard zones should be identified, and
522 corresponding disaster reduction measures should be developed (Cui and Guo, 2021). Moreover,
523 specific structural measures are urgently needed. First, engineering measures should be
524 implemented in the watershed to mitigate debris flows (Cui and Lin, 2013). Second, buildings
525 should not be constructed near debris flow gullies, and new buildings should be built on elevated
526 ground or at certain elevations above the ground (Attems et al., 2019). Third, deflection walls
527 should be considered and constructed in villages susceptible to debris flows to protect entire
528 buildings (Wang et al., 2022), and flood protection walls should be built along the main river to
529 protect the entire flood-prone village.

530 7 Conclusions

531 Buildings in the confluence zone of a debris flow-prone catchment and along a main river
532 channel are highly vulnerable to a debris flow-dam-burst flood hazard chain. Assessing building
533 damage is essential for risk mitigation and resilient construction. However, research concerning
534 building damage mainly focuses on a single debris flow or flash flood and fails to consider the
535 different damage characteristics of buildings exposed to both hazards simultaneously. Therefore,
536 studying the characteristics and patterns of building damage in confluence areas can help to
537 develop a reliable vulnerability assessment method. In this study, we investigate the dynamic
538 characteristics of the hazards and damage patterns of the 2020 Heixiluo debris flow and dam-
539 burst flood disaster. We draw the following conclusion:

540 1. The dam-burst flood, which had a peak discharge of 2,273 m³/s, seriously eroded the debris
541 flow fan and formed a new straighter and steeper channel. The maximum estimated velocity was
542 8.24 m/s, and the bed shear stress reached 853 Pa. The flood's inundation extent in the confluence
543 zone was expanded by a factor of 4, and the impact pressure increased up to 6.76 times due to
544 flood amplification.

545 2. The damage patterns of the buildings were classified into three types: (I) buried by primary
546 debris flow, (II) inundated by secondary dam-burst flood, and (III) buried by debris flow and
547 inundated by dam-burst flood sequentially. Three corresponding hazard zones were identified.
548 The damage to buildings in Zone (III) was 20 times more intense due to the dam-burst flood. The
549 spatial division of hazard zones can be applied to the selection of building sites and to the
550 planning of structural measures in the confluence area.

551 3. The vulnerability curves show a similar increasing trend with impact pressure and
552 inundation depth in Zones II and III, and the threshold of the impact pressures in Zones II and III



553 where vulnerability is equal to 1 are 88 kPa and 106 kPa, respectively. A vulnerability assessment
554 chart was developed, and three categories, namely, slight damage (0.3-0.4), moderate damage
555 (0.6-0.7), and heavy and complete damage (0.8-1.0), were identified. Heavy damage occurs at an
556 impact pressure greater than 40 kPa, while slight damage occurs below 20 kPa. Moderate damage
557 occurs at an impact pressure between 20 kPa and 40 kPa.

558 4. Some uncertainties and limitations are involved in vulnerability analysis. The building's
559 physical characteristics, such as shape, orientation, and maintenance condition, should be
560 considered for the vulnerability analysis. Further investigation and research are recommended to
561 explore the cumulative effect of multiple hazards on building vulnerability. Despite the
562 deficiencies, vulnerability curves and assessment charts are valuable to analyze the risk posed by
563 debris flow hazard chains within the confluence zone.

564

565 **Acknowledgements**

566 This work has been financially supported by the the Second Tibetan Plateau Scientific Expedition
567 and Research Program (2019QZKK0902) and the National Natural Science Foundation of China
568 (41790434).

569

570 **Data availability**

571 All raw data can be provided by the corresponding authors upon request.

572

573 **Author contributions**

574 Kaiheng Hu contributed to the conception of the study; Li Wei performed the data analyses and
575 wrote the manuscript draft; Shuang Liu performed the data analyses. Nan Ning, Xiaopeng Zhang
576 and Qiyuan Zhang performed the field investigation; Md Abdur Rahim reviewed and edited the
577 manuscript.

578

579 **Competing interests.**

580 The authors declare that they have no conflict of interest.

581

582



583 **References**

- 584 Argyroudis, S. A., Mitoulis, S. A., Winter, M. G., and Kaynia, A. M.: Fragility of transport assets exposed
585 to multiple hazards: State-of-the-art review toward infrastructural resilience, *Reliability Engineering*
586 *and System Safety*, 191, 106567, <https://doi.org/10.1016/j.ress.2019.106567>, 2019.
- 587 Arrighi, C., Mazzanti, B., Pistone, F., and Castelli, F.: Empirical flash flood vulnerability functions for
588 residential buildings. *SN Applied Sciences*, 2, 904, <https://doi.org/10.1007/s42452-020-2696-1>, 2020.
- 589 Attems, M. S., Thaler, T., Genovese, E., and Fuchs, S.: Implementation of property-level flood risk
590 adaptation (PLFRA) measures: Choices and decisions. *Wiley Interdisciplinary Reviews, Water*, 7(1),
591 e1404, <https://doi.org/10.1002/wat2.1404>, 2020.
- 592 Chen, H., Ruan, H., Chen, J., Li, X., and Yu, Y.: Review of investigations on hazard chains triggered by
593 river-blocking debris flows and dam-break floods, *Frontiers in Earth Science*, 10, 582.
594 <https://doi.org/10.3389/feart.2022.830044>, 2022.
- 595 Costa, J.E.: *Floods from Dam Failures*, Open-File Rep. No. 85–560. U.S. Geological Survey, Denver, 1985.
- 596 Cui P., and Guo J.: Evolution models, risk prevention and control countermeasures of the valley disaster
597 chain, *Advanced Engineering Sciences*, 53(3), 5-18 <https://doi.org/10.15961/j.jsuese.202100285>, 2021.
- 598 Cui, P., and Lin, Y.M.: Debris-flow treatment: The integration of botanical and geotechnical methods,
599 *Journal of Resources and Ecology*, 4(2), 97-104. <https://doi.org/10.5814/j.issn.1674-764x.2013.02.001>,
600 2013.
- 601 Gallina, V., Torresan, S., Critto, A., Sperotto, A., Glade, T., and Marcomini, A.: A review of multi-risk
602 methodologies for natural hazards: Consequences and challenges for a climate change impact
603 assessment, *Journal of environmental management*, 168, 123-132,
604 <https://doi.org/10.1016/j.jenvman.2015.11.011>, 2016.
- 605 Gautam, D., and Dong, Y.: Multi-hazard vulnerability of structures and lifelines due to the 2015 Gorkha
606 earthquake and 2017 central Nepal flash flood. *Journal of Building Engineering*, 17, 196-201.
607 <https://doi.org/10.1016/j.jobe.2018.02.016>, 2018.
- 608 He, Y. B., Xu, Y.N. and Zhang, J.: Analysis of flood control effect of Pubugou Reservoir during “20•8”
609 flood of Minjiang River, Yangtze River, 51(12):149-154, <https://doi.org/10.16232/j.cnki.1001-4179.2020.12.027>, 2020.
- 611 Hu, K. H., Cui, P., and Zhang, J. Q.: Characteristics of damage to buildings by debris flows on 7 August
612 2010 in Zhouqu, Western China, *Natural Hazards and Earth System Sciences*, 12(7), 2209-2217.
613 <https://doi.org/10.1016/10.5194/nhess-12-2209-2012>, 2012.
- 614 Hu, G., Tian, S., Chen, N., Liu, M., and Somos-Valenzuela, M.: An effectiveness evaluation method for
615 debris flow control engineering for cascading hydropower stations along the Jinsha River, China,
616 *Engineering Geology*, 266, 105472, <https://doi.org/10.1016/j.enggeo.2019.105472>, 2020.
- 617 Hydrologic Engineering Center: HEC-RAS, River Analysis System, *Hydraulics Reference Manual*,
618 Version. 5.0. Davis, California, U.S. Army Corps of Engineers 25 (2016).



- 619 Kang, H. S., and Kim, Y. T.: The physical vulnerability of different types of building structure to debris
620 flow events, *Natural Hazards*, 80, 1475-1493, <https://doi.org/10.1007/s11069-015-2032-z>, 2016.
- 621 Kang, Z.C., Li, Z.F., Ma, A.N.: *Debris flows in China*. Science, Beijing(in Chinese), 2004.
- 622 Kang, Z.C.: A velocity research of debris flow and its calculating method in China, *Mountain Research*, 5
623 (4), 247–259, 1987. (in Chinese).
- 624 Kappes, M. S., Keiler, M., von Elverfeldt, K., and Glade, T.: Challenges of analyzing multi-hazard risk: a
625 review, *Natural hazards*, 64, 1925-1958. <https://doi.org/10.1007/s11069-012-0294-2>, 2012.
- 626 Korswagen, P. A., Jonkman, S. N., and Terwel, K. C.: Probabilistic assessment of structural damage from
627 coupled multi-hazards, *Structural safety*, 76, 135-148, <https://doi.org/10.1016/j.strusafe.2018.08.001>,
628 2019.
- 629 Li, N. D., Liu, W., and Zhao, J. H.: Behavioural analysis and dynamic simulation of the debris flow that
630 occurred in Ganluo County (Sichuan, China) on 30 August 2020, *Journal of Mountain Science*, 19(6),
631 1495-1508, <https://doi.org/10.1007/s11629-021-7199-z>, 2022.
- 632 Liu, Z., Nadim, F., Garcia-Aristizabal, A., Mignan, A., Fleming, K., and Luna, B. Q.: A three-level
633 framework for multi-risk assessment, *Georisk: Assessment and management of risk for engineered*
634 *systems and geohazards*, 9(2), 59-74, <https://doi.org/10.1080/17499518.2015.1041989>, 2015.
- 635 Luo, H. Y., Zhang, L. M., Zhang, L. L., He, J., and Yin, K. S.: Vulnerability of buildings to landslides, The
636 state of the art and future needs. *Earth-Science Reviews*, 104329,
637 <https://doi.org/10.1016/j.earscirev.2023.104329>, 2023.
- 638 Luo, H., Zhang, L., Wang, H., and He, J.: Multi-hazard vulnerability of buildings to debris flows,
639 *Engineering Geology*, 279, 105859, <https://doi.org/10.1016/j.enggeo.2020.105859>, 2020.
- 640 Ning, L., Hu, K., Wang, Z., Luo, H., Qin, H., Zhang, X., and Liu, S.: Multi-hazard chain reaction initiated
641 by the 2020 Meilong debris flow in the Dadu River, Southwest China. *Frontiers in Earth Science*, 10,
642 827438, <https://doi.org/10.3389/feart.2022.827438>, 2022.
- 643 Park, S., van de Lindt, J. W., Cox, D., Gupta, R., and Aguiniga, F.: Successive earthquake-tsunami analysis
644 to develop collapse fragilities, *Journal of Earthquake Engineering*, 16(6), 851-863,
645 <https://doi.org/10.1080/13632469.2012.685209>, 2012.
- 646 Petit, F., Houbrechts, G., Peeters, A., Hallot, E., Van Campenhout, J., and Denis, A. C.: Dimensionless
647 critical shear stress in gravel-bed rivers, *Geomorphology*, 250, 308-320.
648 <https://dx.doi.org/10.1016/j.geomorph.2015.09.008>, 2015.
- 649 Petrone, C., Rossetto, T., Baiguera, M., De la Barra Bustamante, C., and Ioannou, I.: Fragility functions for
650 a reinforced concrete structure subjected to earthquake and tsunami in sequence, *Engineering*
651 *Structures*, 205, 110120, <https://doi.org/10.1016/j.engstruct.2019.110120>, 2020.
- 652 Quan, L.B., Blahut, J., van Westen, C.J., Sterlacchini, S., van Asch, T.W.J., Akbas, S.O.: The application
653 of numerical debris flow modelling for the generation of physical vulnerability curves, *Natural*
654 *Hazards and Earth System Sciences*, 11, 2047-2060, <https://doi.org/10.5194/nhess-11-2047-2011>,
655 2011.



- 656 Tilloy, A., Malamud, B. D., Winter, H., and Joly-Laugel, A.: A review of quantification methodologies for
657 multi-hazard interrelationships, *Earth-Science Reviews*, 196, 102881,
658 <https://doi.org/10.1016/j.earscirev.2019.102881>, 2019.
- 659 Wang, J., Hassan, M. A., Saletti, M., Yang, X., Zhou, H., and Zhou, J.: Experimental study on the
660 mitigation effects of deflection walls on debris flow hazards at the confluence of tributary and main
661 river, *Bulletin of Engineering Geology and the Environment*, 81(9), 354.
- 662 Wei, L., Hu, K., and Liu, J.: Automatic identification of buildings vulnerable to debris flows in Sichuan
663 Province, China, by GIS analysis and Deep Encoding Network methods, *Journal of Flood Risk
664 Management*, 15(4), e12830, <https://doi.org/10.1111/jfr3.12830>, 2022.
- 665 Xu, L., Meng, X. and Xu, X.: Natural hazard chain research in China: A review, *Natural Hazards* 70, 1631-
666 1659, <https://doi.org/10.1007/s11069-013-0881-x>, 2014.
- 667 Yan, Y., Cui, Y., Liu, D., Tang, H., Li, Y., Tian, X., Zhang, L., and Hu, S.: Seismic signal characteristics
668 and interpretation of the 2020 “6.17” Danba landslide dam failure hazard chain process, *Landslides*,
669 18, 2175–2192 (2021). <https://doi.org/10.1007/s10346-021-01657-x>, 2021.
- 670 Yang, Z.N., 1985. Preliminary study on the flowing velocity of viscous debris flows due to intense rainfall,
671 Research of debris flows, *Proceeding of the Lanzhou Institute of Glaciology and Cryopedology*,
672 Chinese Academy of Sciences. No. 4. Science Press, Beijing (in Chinese).
- 673 Yu, B., Ma, Y., and Wu, Y. (2013). Case study of a giant debris flow in the Wenjia Gully, Sichuan
674 Province, China, *Natural Hazards*, 65, 835-849. <https://doi.org/10.1007/s11069-012-0395-y>, 2013.
- 675 Zanchetta, G., Sulpizio, R., Pareschi, M. T., Leoni, F. M., and Santacroce, R.: Characteristics of May 5-6,
676 1998 volcanoclastic debris flows in the Sarno area (Campania, southern Italy): relationships to
677 structural damage and hazard zonation, *Journal of volcanology and geothermal research*, 133(1-4),
678 377-393, [https://doi.org/10.1016/S0377-0273\(03\)00409-8](https://doi.org/10.1016/S0377-0273(03)00409-8), 2004.
- 679 Zhang, S., Zhang, L., Li, X., and Xu, Q.: Physical vulnerability models for assessing building damage by
680 debris flows, *Engineering Geology*, 247, 145-158 <https://doi.org/10.1016/j.enggeo.2018.10.017>, 2018.
- 681